Transient optical response of ultrafast nonequilibrium excited metals: Effects of electron-electron contribution to collisional absorption

J. P. Colombier,[1] P. Combis,[2] E. Audouard,[1] and R. Stoian[1]
[1]*Laboratoire Hubert Curien, Université Jean Monnet, UMR CNRS 5516, 18 rue Benoît Lauras, 42000 Saint-Etienne, France*
[2]*Département de Physique Théorique et Appliquée, CEA/DAM Ile de France, 91297 Arpajon, France*
(Received 20 December 2007; published 27 March 2008)

Approaching energy coupling in laser-irradiated metals, we point out the role of electron-electron collision as an efficient control factor for ultrafast optical absorption. The high degree of laser-induced electron-ion nonequilibrium drives a complex absorption pattern with consequences on the transient optical properties. Consequently, high electronic temperatures determine largely the collision frequency and establish a transition between absorptive regimes in solid and plasma phases. In particular, taking into account umklapp electron-electron collisions, we performed hydrodynamic simulations of the laser-matter interaction to calculate laser energy deposition during the electron-ion nonequilibrium stage and subsequent matter transformation phases. We observe strong correlations between optical and thermodynamic properties according to the experimental situations. A suitable connection between solid and plasma regimes is chosen in accordance with models that describe the behavior in extreme, asymptotic regimes. The proposed approach describes as well situations encountered in pump-probe types of experiments, where the state of matter is probed after initial excitation. Comparison with experimental measurements shows simulation results which are sufficiently accurate to interpret the observed material behavior. A numerical probe is proposed to analyze the transient optical properties of matter exposed to ultrashort pulsed laser irradiation at moderate and high intensities. Various thermodynamic states are assigned to the observed optical variation. Qualitative indications of the amount of energy coupled in the irradiated targets are obtained.

DOI: 10.1103/PhysRevE.77.036409 PACS number(s): 52.25.Fi, 61.80.Az, 72.15.Cz, 79.20.Ap

I. INTRODUCTION

Laser-induced phase transitions are extensively investigated by means of optical measurements due to their fundamental interest and potential in material sciences and engineering. Optical probing was identified as a relatively straightforward way to time-resolve the changes of material properties. However, singular effects in the material response in extreme conditions are not always easy to identify in the sequence of matter alterations [1–5]. Although more accurate measurements using x-ray or electron diffraction have emerged to probe matter transformation with atomic resolution [6,7], optical probing is still a powerful technique to resolve evolution changes in material transformations in a wide range of thermodynamical states. First, investigations of ultrashort-pulsed laser energy relaxation in metals concentrated on a wide range of effects including pump-probe reflection and transmission efficiencies [8] and time-resolved particle emission and two-photon photoemission experiments [9]. Subpicosecond lasers have been used to resolve nonequilibrium heating in Au and Cu [10,11] and to measure the electron-phonon coupling for a variety of metals [12,13]. Modeling the correct behavior of the material properties under strong excitation is still a challenge for understanding transport properties and relaxation processes in nonequilibrium systems [14–16]. Irradiated by an intense laser beam, a material undergoes a complex series of transformations, from solid-solid, solid-liquid, liquid-gas, up to the plasma phase. Each transformation has a particular optical signature, and the description of the evolution remains a fundamental issue [17–20]. Hence, comparison of experiments with dedicated models is needed to validate the modeling approach even though experiments on extreme conditions of matter are difficult to perform and the data are scarce and often contradictory. Nevertheless, since experiments involve complex interconnected phenomena, various models with different degrees of complexity are required to decode the experimental information.

A specificity of ultrafast laser excitation is its highly transient nature. Ultrafast laser irradiation can push matter in extreme high-pressure, high-temperature, nonequilibrium states where hot electrons interact with colder ions [21]. Hereby, nonequilibrium describes the temperature mismatch between hot electrons and ions, while each interacting subsystem is considered thermalized on the time scales involved. If this is a crude approximation in the first moments of interaction, the establishment of a high collision rate will reduce the domain of incertitude. Subsequently, the properties of the material are governed by the relaxation paths toward the equilibrium state [22]. Moreover, since optical probing only involves the electronic system, information on lattice structural changes must be inferred indirectly from changes in the electronic system. From a fundamental and theoretical point of view, interesting features emerge when the pulse width becomes shorter than the electron-phonon relaxation time scale for energy deposition into the solid [23]. For this reason, we will be approaching systems whose dynamical evolution exhibits a pattern driven by the electron-electron and electron-ion collisional interactions (such as reflectivity or absorption coefficients). The energy distribution among each species determines changes within the excited material which affect the relative transport properties. Since optical properties depend strongly on the ionization degree which is in turn controlled by temperature and

density evolution, a hydrodynamic approach is required. A coupled electromagnetic and hydrodynamic formalism, associated with specific optical and thermal models reflecting nonequilibrium features, provides an effective way to reproduce laser-matter experiments. Such simulations have been performed using the ESTHER code, developed by the Commissariat à l'Energie Atomique, France. Details of the code assumptions and approaches are given in Refs. [24,25] and will be briefly reviewed in the next sections, focused on an absorption and thermodynamic description.

A full theoretical description of the solid-laser interaction requires a self-consistent treatment of hydrodynamics and the evolution of the transport properties which are associated with it. Despite many efforts, a global view including the multitude of interaction and relaxation processes is still incomplete and only particular aspects are understood at this time. The analysis of the transient optical properties of a laser-induced dense nonequilibrium plasmas requires a description of electron degeneracy effects. Different approaches have been used to model interaction mechanisms and subsequent energy absorption. For considering the role of these interactions on degenerate matter properties, ionic and electronic structure effects in relation to transport properties have to be calculated [26–29]. Some of the studies dealing with ultrafast absorption phenomena are focused on the complex effect of a simultaneous contribution of collision processes on the kinetic equation [16,30,31]. In considering the nonequilibrium dynamics of electrons in metals, the mutual influence of $(e\text{-}e)$ and $(e\text{-}p)$ interactions remains an issue of interest. Although quantum mechanical approaches and kinetic treatments have been developed to characterize the absorption rate in dense plasmas and solids [32–34] and significant progress has been made, the formulation of electron excitation through all these regimes remains difficult and limited. Consequently, we concentrate our calculations on the effects resulting from bringing together basic models to discriminate dominant mechanisms in several experimental situations, encompassing a large variety of thermodynamic states. For excitation below certain relaxation times (electron-phonon equilibration), nonequilibrium appears, particularly in the femtosecond excitation regime. The dominant effects on the nonlinear optical dynamics arrive from the Pauli exclusion principle and the Coulomb electron-electron interactions among the free carriers $(e\text{-}e)$. The phonons also play an important role, especially on picosecond time scales. During and following their excitation, the electrons undergo a number of different relaxation stages as they scatter among themselves via the Coulomb interaction and with the phonons via the electron-phonon $(e\text{-}p)$ interaction. In optical absorption, a contribution may appear from electronic processes that allows momentum variation and conductivity changes. The $(e\text{-}e)$ interaction contributes indirectly to the inverse bremsstrahlung process of absorption since it screens the electron-ion pseudopotential and directly via umklapp processes. For simplicity and according to some other investigations dedicated to optical probing [14,35,36], we adopt a phenomenological approach as being well suited for integration in hydrodynamic codes. In this natural way, collision rates are described under the relaxation-time approximation for both $(e\text{-}e)$ and $(e\text{-}p)$ [37]. Obviously, this simplified approach cannot describe specific features of the collision process, but along with different kind of experiments, it is adequate to improve *ad hoc* transport models in solid material up to the plasma phase. This will help to reproduce the transient evolution of the optical properties. By measuring the amplitude of the optical field emerging from the irradiated sample upon reflection, one can gain valuable insight into the interplay between many-body interactions and quantum confinement effects during very short time scales.

The aim of this paper is to provide a deeper insight into the transport characteristics and their consequence on the optical properties in nonequilibrium systems, such as ultrashort laser-excited metals. With support of numerical calculations, we concentrate our investigations on several issues. First of all, the effect of electron-electron collision on the transient optical properties is modeled. Our original motivation was to insert a more accurate description of the laser absorption in the ESTHER code. In order to validate our modeling assumptions, we perform simulations of reflectivity dependence on the angle of incidence, polarization, and intensity while comparing the results with experimental data available in the literature [38,39]. Our results reveal that the calculations match the experimental data with great accuracy when considering the effect of $(e\text{-}e)$ collision rate enhancement during laser irradiation. To extend our investigations, a great challenge is to compare the time evolution of the calculated optical properties with time-resolved experiments. In fact, with subpicosecond laser pulses, it is also possible to probe in a time-resolved fashion the charge carrier dynamics in metals by a pump-probe optical system. Recent measurements on reflectivity and transmittivity evolution under ultrafast laser irradiation in pump-probe types of experiments have been reported [5]. To realize a similar numerical pump-probe experiment, further developments are required to identify potentially induced phenomena in the framework of an optical, thermal, and hydrodynamical study. Straightforward numerical modeling of such problems is a difficult challenge due to the various natures of underlying physical phenomena. While performing an analysis of the measured optical properties, we propose an interpretation of the results by splitting the behavior into two stages: a dense and nonequilibrium plasma phase following by a hot expanded plasma regime. Our laser-matter numerical tool demonstrates new abilities to investigate nonequilibrium and associated collisional effects on the material states ranging from cold solid to hot plasma.

The rest of this paper is organized as follows. We first detail the modeling of the laser absorption by the material in Secs. II and III. In Sec. IV, we make use of a comparison with available experimental data sets to validate our numerical modeling. We then broaden the range of simulation by investigating the electromagnetic interactions relative to pump-probe numerical experiments. These experiments, ranging from high intensities to below ablation threshold excitation, furnish arguments that demonstrate the applicability of such a numerical tool. Conclusions are drawn in the last section.

II. ELECTROMAGNETIC EXCITATION BY ULTRASHORT LASER PULSES

A. Laser-matter interaction background

When electromagnetic irradiation is shorter than several picoseconds, the equilibration time between the solid lattice and the laser-heated electrons is longer than the laser pulse length. Thus, thermal equilibrium could not be ensured and the thermal state of the solid lattice is not well known. In order to understand the complexity of material absorption under the laser irradiation, the modeling of laser-matter interactions requires the interconnection of different physics fields, including optics, heat transfer, fluid dynamics, and phase transitions in nonequilibrium frames. Among different models that treat the interaction between ultrafast laser light and metallic targets at moderate intensities and provide scenarios of material ejection [16,40–43], the hydrodynamic approach employing tabulated Bushman-Lomonosov-Fortov [44] multiphase equations of state (EOS) addresses reasonably well the complexity of the problem. It also has the potential to reveal plausible evolution paths for the excited matter that have also relevance for improving the laser interaction process [25,45]. The one-dimensional hydrodynamic code ESTHER includes a two-temperatures model to reproduce electronic thermal diffusion which takes place during electron-ion nonequilibrium. It is extended by a nonequilibrium hydrodynamic model decoupling electron and ion pressure components which both contribute to the ultrafast matter deformation according to the Euler equations. Fluid equations are solved to account for the conservation of energy, momentum, and mass in a Lagrangian formalism. The specificity of this approach is the flexible dimension of the cells which deform together with the material and permit an accurate description of shock propagation. The simulation accounts for mechanical processes and particularly the effects on material strength that occur in shock propagation. This is due to constitutive models which describe the pressure and temperature dependence of shear modulus and yield strength [46]. This code is enhanced with a wave-equation solver to calculate the electromagnetic field in the material during laser-matter interaction. To determine the optical response, especially in the presence of a density gradient, Maxwell equations are reduced to the Helmholtz equation by using a slowly varying envelope approximation for the electric field. This is justified because, for a laser pulse of $\tau = 150$ fs, the wavelength $\lambda = 800$ nm is smaller than the coherence length $L_\tau = c\tau$, where c is the speed of light.

B. Optical property modeling

If the idealized density step profile is no longer actual, the Fresnel equations cannot be used and it becomes necessary to calculate the absorption in a nonuniform density profile. The electric field is calculated numerically by solving the wave equation, using a one-dimensional mesh. The cell coordinates evolve in time due to the Lagrangian approach used to solve the hydrodynamic equations. For two pulses excitation, the contribution of each pulse is accounted for. The subscript α refers to the pump laser field at the frequency ω_α, and β refers to the probe one at the frequency ω_β. We consider a planar wave propagating along the z axis. We denote ϑ the angle which the normal to the wave makes with the z axis. Each component (x,y,z) of the electric field is defined by the equation $\tilde{\mathcal{E}}^{x,y,z}_{\alpha,\beta} = \tilde{A}^{x,y,z}_{\alpha,\beta}(z)\exp(ik^0_{\alpha,\beta}x \sin\theta)$ where $k^0_{\alpha,\beta} = \omega_{\alpha,\beta}/c$ is the vacuum wave number. We write the following Helmholtz equation which is solved 2 times for the complex amplitudes of each components (α,β) of the electric fields:

$$\frac{\partial^2 \tilde{A}^{x,y,z}_{\alpha,\beta}}{\partial z^2} + \tilde{k}^2_{\alpha,\beta}\tilde{A}^{x,y,z}_{\alpha,\beta} = 0. \tag{1}$$

Here, the complex vector $\tilde{k}$ depends on the dielectric function ϵ:

$$\tilde{k}^2_{\alpha,\beta} = (k^0_{\alpha,\beta})^2[\epsilon - \sin^2\vartheta]. \tag{2}$$

In the solid case, the complex vector $\tilde{k}$ is defined as a function of the refractive index η and the extinction coefficient κ:

$$\tilde{k}^2_{\alpha,\beta} = (k^0_{\alpha,\beta})^2[(\eta_{\alpha,\beta} - i\kappa_{\alpha,\beta})^2 - \sin^2\vartheta_{\alpha,\beta}]. \tag{3}$$

η and κ are taken at room temperature as a function of the wavelength from Ref. [47].

When the density decreases at the metal surface, the optical properties are strongly different from the above values and the electrical conductivity $\tilde{\sigma}$ for dense metal plasma at the equilibrium temperature is determined using the tabulated values given in Ref. [48]. Experimental measurements of the electrical conductivity of dense copper and aluminum plasmas in the equilibrium temperature range of several eV and for a density range from the solid density down to 0.01 g/cm^3 [49] have been compared with theoretical models for conductivity by Ebeling *et al.* [48]. We used the resultant σ_{dc} and the ionization rate under a tabulated form for given electron density and temperatures in our calculation. A phenomenological collision frequency is deduced from these values to determine the collision frequency at equilibrium $\nu_{eq}(N_e, T_e = T_i)$. It has to be noted that an interpolation is performed between the solid and plasma phases for intermediate regime. For the liquid, gas, and plasma cases, the dielectric function is given by the Drude model and Eq. (2) becomes

$$\tilde{k}^2_{\alpha,\beta} = (k^0_{\alpha,\beta})^2\left(1 - \sin^2\vartheta_{\alpha,\beta} - \frac{i\tilde{\sigma}_{\alpha,\beta}}{\omega_{\alpha,\beta}\varepsilon_0}\right). \tag{4}$$

Here, ε_0 is the vacuum dielectric permittivity.

C. Reflectivity and transmissivity calculations

The reflectivity $\mathcal{R}^{p,s}$, where (p,s) denotes the polarization state, is determined in a general manner, by calculating the ratio between the reflected and the incident power. The transmissivity $\mathcal{T}^{p,s}$ is evaluated by the ratio between the transmitted and the incident power. The absorptivity is determined by the ratio between the absorbed and the incident power. The relation $\mathcal{T}^{p,s} = 1 - \mathcal{R}^{p,s} - \mathcal{A}^{p,s}$ is satisfied. The angle dependence of the incident laser absorption is an important factor for a good optimization of the interaction. In this numerical

experiment, the reflection factor is determined as the averaged value integrated on the measurement time. The calculation is realized by weighting the incident intensity with the following form:

$$\overline{\mathcal{R}^{p,s}_{\alpha,\beta}}(\tau) = \frac{\int_0^\tau \mathcal{R}^{p,s}_{\alpha,\beta}(t)|\mathcal{E}^{p,s}_{\alpha,\beta}(t)|^2 dt}{\int_0^\tau |\mathcal{E}^{p,s}_{\alpha,\beta}(t)|^2 dt}, \tag{5}$$

$$\overline{\mathcal{T}^{p,s}_{\alpha,\beta}}(\tau) = \frac{\int_0^\tau \mathcal{T}^{p,s}_{\alpha,\beta}(t)|\mathcal{E}^{p,s}_{\alpha,\beta}(t)|^2 dt}{\int_0^\tau |\mathcal{E}^{p,s}_{\alpha,\beta}(t)|^2 dt}. \tag{6}$$

As mentioned, simulation results are obtained in performing pump-probe numerical experiments during which the Helmholtz equations are solved for both pump and probe pulses. In this context, the reflectivity and transmissivity can be associated with distinctive wavelengths corresponding to each kind of pulse. In fact, material optical indices evolve as a function of the corresponding wavelength in time for each pulse. In the ESTHER code, both reflectivity and transmissivity are calculated at each time step δt of the simulation. This allows for, according to the specific type of experiment, these parameters either to be integrated over the duration of the pulse or to give momentary values. In the former case, $\tau = \tau_L$ is used for the integral up boundary. For experiments providing data resolved in time below the picosecond time scale, $\tau = \delta t$ has been used in the previous expressions.

D. Absorption collisional aspects in stages subsequent to excitation

Electrons interact via the bare Coulomb interaction, and after time intervals of the order of the inverse plasmon frequency corresponding to the relevant carrier density, the interactions become screened. Immediately after the photon absorption phase, collisions among electrons cause loss of coherence and a hot population of electrons is formed. Electrons and ions are initially described by two independent populations. The electrons evolve into hot thermal distributions characterized by an electron temperature that can exceed significantly that of the lattice. Such a time evolution, as the carriers equilibrate among themselves, is mainly induced by the $(e\text{-}e)$ and $(e\text{-}p)$ interaction. The duration of this stage is determined by the energy relaxation time, which can be of the order of picoseconds. The carrier dynamics affects the absorption properties through the conductivity parameter. In a first approximation, this quantity is completely described by the frequency-dependent Drude contribution

$$\tilde{\sigma}^D_{\alpha,\beta} = \frac{N_e e^2}{m_e^\dagger} \frac{\nu + i\omega_{\alpha,\beta}}{\nu^2 + \omega^2_{\alpha,\beta}}, \tag{7}$$

where the collision frequency ν is given by the sum of the electron-electron (ν^{ee}) and electron-ion (ν^{ei}) contributions. We can therefore express the collision frequency as a sum of equilibrium and nonequilibrium contributions:

$$\nu = \nu_{eq} + \nu_{neq} = \nu_{eq}(N_e, T_i) + \nu_{neq}(N_e, T_e) - \nu_{neq}(N_e, T_e = T_i). \tag{8}$$

Here, $\nu_{eq}(N_e, T_i)$ and $\nu_{neq}(N_e, T_e = T_i)$ are $(e\text{-}i)$ collision frequencies at equilibrium, calculated in two different ways. The first term is determined using the tabulated values of conductivity at equilibrium [48]. These tabulated values were shown to match well experimental situations [49]. The last term corresponds to the equilibrium contribution to the collision frequency calculated by our nonequilibrium model. To ensure a convergence toward tabulated equilibrium values, we subtract the equilibrium contribution from the nonequilibrium one. In this manner, the contribution of electrons out of equilibrium is treated as a correction of the known values of the equilibrium conductivity. Finally, the second term $\nu_{neq}(N_e, T_e)$ is the nonequilibrium collision frequency for electrons which account for $(e\text{-}e)$ (via umklapp processes) and $(e\text{-}i)$ interactions for an electronic temperature larger than the ionic one. This latter contribution is calculated independently from the former one as it will be seen in the next paragraph.

The electron-electron part is a fundamental issue for the description of low-temperature or nonequilibrium transport phenomena. It is a difficult problem to deal correctly with electron-electron scattering in calculations of transport coefficients. One possible way is the Boltzmann transport equation. However, the Boltzmann transport equation cannot usually be solved exactly and some approximations have to be introduced, such as a relaxation-time approximation. No tractable model exists to describe the conductivity on a large range of temperatures and densities, and we propose an interpolation between the different regimes with established characteristics: the solid and plasma states. To take this into account, we have used an approach based on an interpolation between current solid and plasma models following the approach in Ref. [36]. The relaxation rate $(1/\nu)$ is calculated with the assumption of a screened Coulomb interaction among the electrons. The $(e\text{-}e)$ relaxation rate rises with increasing density until it reaches a maximum after which increasing screening causes the rate to fall. The evolution of the optical properties during an ultrashort laser pulse remains an open question. A complete description of the effect of the $(e\text{-}e)$ collisions would require complete knowledge of both the metal band structure and dense-plasma atomic structure, which makes them analytically complex and unsuitable for the modeling purposes considered here. In reality, it is not quite obvious how electron-electron collisions can induce a conductivity effect in the nonequilibrium solid. For a free electron gas, the parabolic energy-momentum relation for which velocity and momentum are proportional results in neglecting $(e\text{-}e)$ interactions contribution to absorption. The classical approach implies that, since total current and total momentum are proportional, the current is conserved during this type of collisions, which preserves momentum. As a consequence, the conductivity evolution is supposed to be independent of $(e\text{-}e)$ interactions. However, in periodic sys-

tems, as the solid sample in the first moments of interaction, the total momentum involving (e-e) interactions may be conserved via the involvement of a reciprocal lattice vector. This type of process will allow in consequence a variation of the electronic momentum and induces a change in conductivity [50]. A term ν_{neq}^{ee} is then used to correct the conductivity during the nonequilibrium stage. To justify our approach, we expect that umklapp processes can occur at a rate given by a factor Δ with respect of the normal process ($\Delta < 1$) [51,52]. The values of this term (0.4 and 0.35 for aluminum and gold, respectively) have been taken from Refs. [53–55], being derived by low-temperature investigations. These values will be considered constant in this study, although a dependence on the electronic field and collision rates is foreseeable. In taking into account this process, the slowing down of the electron flow can be expected during (e-e) interaction and results in a change in the absorption coefficient when the lattice remains cold, during the first moments of laser irradiation.

At near-solid density and moderate electronic temperature up to few eV, the Fermi gas undergoes collisions and the solid-model is given by [56]

$$\nu_{neq}^{ee} = \frac{\mathcal{C}}{\mathcal{N}} \int_0^\infty d\mathcal{E}(\mathcal{E} - \mathcal{E}_F)^2 f(\mathcal{E}, T_e)[1 - f(\mathcal{E}, T_e)], \tag{9}$$

where $f(\mathcal{E}, T_e)$ is the Fermi-Dirac statistic distribution depending on T_e and N_e through the chemical potential

$$\mathcal{N} = -k_B T_e f(0, T_e),$$

$$\mathcal{C} = \Delta \frac{\mathcal{D}}{\mathcal{E}_{TF}^{3/2} \mathcal{E}_F^{1/2}} \left[\frac{2\sqrt{\mathcal{E}_{TF}\mathcal{E}_F}}{4\mathcal{E}_{TF} + \mathcal{E}_F} + \arctan \sqrt{\frac{4\mathcal{E}_F}{\mathcal{E}_{TF}}} \right],$$

$$\mathcal{E}_{TF} = \frac{\hbar^2 q_{TF}^2}{2m_e^\dagger}, \tag{10}$$

where

$$q_{TF} = \frac{\zeta e}{\pi \hbar} \sqrt{\frac{m_e^\dagger}{\epsilon_0 \epsilon_d}} (3\pi^2 N_e)^{1/6},$$

where $\mathcal{D} = m_e^\dagger e^4 / 64\hbar^3 \pi^3 \epsilon_0^2 \epsilon_d^2$, $m_e^\dagger$ is the effective electron mass [47], Δ is the rate of umklapp processes, and ϵ_d represents the contribution of band d electrons to the static dielectric function in the case of noble metals. In the same way as described in Ref. [56], we have used the screening wave vector q_{TF} containing the adjustable parameter of screening, $\zeta \leq 1$, which was set by fitting the experimental results of these authors. The solid model is applicable up to the Fermi temperature. We assume that the absorption is mainly driven by the free electrons and this model allows us to calculate a straightforward dependence in T_e. This approximation provides a schematic view of the absorption which can be included in the code. For electrons at temperatures around the Fermi value, the phase space available for scattering increases with the electronic temperature due to the Pauli exclusion. Note that the increase in the (e-i) collision frequency due to the T_e augmentation is supposed to be negligible with respect to the (e-e) contribution.

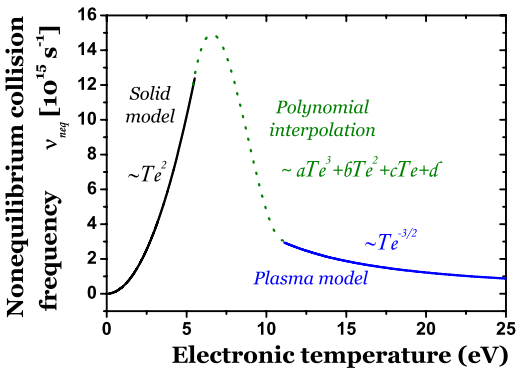

FIG. 1. (Color online) Nonequilibrium collision frequency interpolated in a wide range of electron temperatures in Au. Solid and plasma models (solid lines) are connected by a polynomial interpolation (dashed line) which allows an extension in the unknown regime.

For larger electronic temperatures, we use the plasma collision frequency given by the Spitzer formula

$$\nu_{neq}^{ei} = \frac{\mathcal{E}_F}{\hbar} \left(\frac{k_B T_e}{\mathcal{E}_F} \right)^{-3/2}. \tag{11}$$

The approximations inherent to the plasma model are more acceptable at low density compared to using the solid model at high temperature [57]. To reduce the interpolation range in the unknown region, we suppose that the Spitzer assumptions become suitable for $T_e > 2T_F$. These assumptions may be criticized because of the high density close to the solid one, but the choice of this direct temperature dependence is largely used to represent the global behavior. The nonequilibrium frequency over a large range of temperature is then defined by

$$\nu_{neq} = \nu_{neq}^{ee}(N_e, T_e) \quad \text{for} \quad T_e \leq T_F,$$

$$\nu_{neq} = \nu_{neq}^{int}(N_e, T_e) \quad \text{for} \quad T_F < T_e < 2T_F,$$

$$\nu_{neq} = \nu_{neq}^{ei}(N_e, T_e) \quad \text{for} \quad T_e \geq 2T_F, \tag{12}$$

where $\nu_{neq}^{int} = aT_e^3 + bT_e^2 + cT_e + d$ is a cubic interpolation which offers a realistic continuity between the two models. The interpolated data points are created so that they have a slope equal to the slope of the start or end segments. Note that each term (a,b,c,d) is calculated and tabulated as a function of N_e. Figure 1 shows the nonequilibrium collision frequency interpolated in a wide range of temperatures in Au.

As a conclusion, direct (e-e) contributions to the optical absorption are taken into account via umklapp processes which are supposed to occur in the solid phase via a reciprocal lattice vector. This allows, in turn, a variation of the electronic momentum and, subsequently, a contribution to the optical conductivity. Concerning the (e-i) contribution, the indirect screening of the ion potential by electronic influences is accounted for by the popular Spitzer dependence of the nonequilibrium collision frequency. The equilibrium conductivity values are derived from theoretical considerations which match experimental conductivity results. We suppose

that the electric field influence is taken into account indirectly by the effect of the electronic energy on the collision rate. In this way, the nonequilibrium ($T_e \ll T_i$) affects the Joule heating in the condensed phase in considering the contribution of (e-e) collisions. Although interpolation between solid and plasma regimes is questionable, we suppose that (e-e) effects prevail during the laser-solid interaction, yielding a dramatically modified scaling $\nu_{neq} \propto T_e^2$ [58]. A strong influence of this law is expected on the laser absorption, which will be discussed in the next sections.

E. Interband contribution

The absorption model was implemented for two metallic materials: gold and aluminum. For gold, no specific model of nonequilibrium interband contribution was implemented. We assume that the equilibrium contribution of the collision frequency already contains interband aspects. Moreover, it is supposed that the contribution of d bands in the case of noble metals was taken into account in Eq. (10).

For aluminum, the dielectric constant of the metal takes into account two mechanisms of laser energy deposition: intraband absorption in the sp band and interband absorption (parallel band). Intraband absorption is described through the Drude model, while the Ashcroft-Sturm model is used for the interband contribution [59]. The influence of the interband transition in aluminum conductivity is then considered as $\tilde{\sigma} = \tilde{\sigma}^D + \tilde{\sigma}^{IB}$. Fisher *et al.* have reported theoretical and experimental investigations of aluminum absorption for femtosecond laser irradiation in showing the influence of the interband and intraband (Drude) contributions at 400 and 800 nm [36]. These results were verified in conducting a comparable model of interband effects on the conductivity and similar results were obtained by our numerical code.

III. EXPERIMENTAL VALIDATION OF THEORETICAL MODEL

In order to validate our simulations with experimental results, this section is dedicated to a comparison between selected literature data and numerical calculations based on the present model of ultrafast laser absorption. The experimental part focuses on two demonstrations: two kinds of experiments were reproduced to investigate the optical properties of high-density plasmas. Studies of the absorption dependence in the angle of incidence and intensity were performed. Moderate and high intensities were considered for uv ultrashort laser pulses. The results provide optical properties in both solid and high-density plasma ranges during the laser pulse.

Fedosejevs *et al.* [38] have measured the averaged reflectivity corresponding of a KrF laser pulse of 250 fs at 248 nm focused on aluminum samples as a function of the polarization and the angle of incidence for two intensities: 10^{14} W/cm^2 and 2.5×10^{15} W/cm^2. At the higher intensity, the prepulse is supposed to be sufficiently intense to produce a preplasma at the metal surface. In fact, the absorption of the main pulse is strongly modified by the preplasma occurrence. In this condition we restrain our study to the lower-intensity experiment, which corresponds to a laser fluence of 25 J/cm^2. The experimental measurements were performed to demonstrate the characteristic angular dependence of electromagnetic absorption expected for the extremely steep density gradients of plasmas. Our calculations can be compared with the experimental data since we solve the wave equation for nonstationary density and temperature profiles. If the absorptivity decreases with the angle of incidence for the s polarization, a maximum absorptivity around 62% for the p polarization was observed for an angle of $(54 \pm 3)°$. This corresponds to the maximum energy deposited in the material. In the experiment, the incident beam has a nondesired mixed polarization and the intensity corresponding to a p polarization is in fact composed of 93% p polarization and 7% s polarization. The inverse ratio corresponds to s polarization. This polarization state was entered in our simulations, and the calculated reflectivity is given as a function of the parameter of polarization x_p, which has been fixed to be equal at 0.86 in the p-polarization case and −0.86 in the s-polarization case:

$$\overline{\mathcal{R}_\alpha} = \frac{1}{2}[(1 + x_p)\overline{\mathcal{R}_\alpha^p} + (1 - x_p)\overline{\mathcal{R}_\alpha^s}]. \tag{13}$$

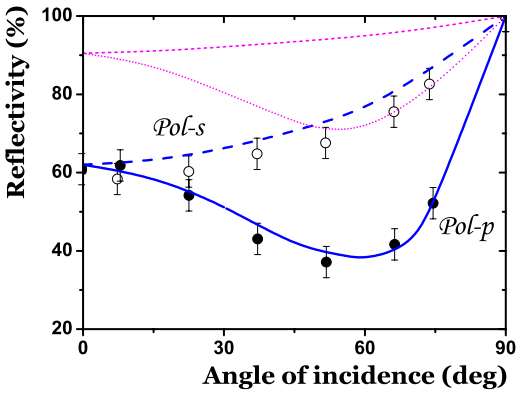

FIG. 2. (Color online) Simulated reflectivity as a function of angle of incidence for a 250-fs, 248-nm laser pulse for s-polarized (dashed line) and p-polarized (solid line) irradiation of an aluminum target at 10^{14} W/cm^2 intensity. Minimal reflectivity is obtained for an angle of $(59 \pm 3)°$. Simulations performed with $\nu_{neq}=0$ are superposed for s (short-dashed line) and p (dotted line) polarization. Experimental data points [open (s) and solid (p) circles with error bars] are taken from Fedosejevs *et al.* [38].

Figure 2 shows the reflectivity as a function of the angle of incidence for both polarizations. The simulated values were calculated with the expressions (5) and (13) with $\tau_L = 750$ fs corresponding to the total pulse duration. The simulations were performed with the expression (8) for dominantly p polarization (solid curve) and s polarization (dashed curve). To show the influence of the nonequilibrium absorption term and especially the (e-e) collision effects, other simulation results are represented by setting the nonequilibrium contribution to ν equal to zero. Expression (8) is reduced to the first equilibrium term which only depends on N_e and T_i ($\nu_{neq}=0$). These simulations have been done for p polarization (short-dotted curve) and s polarization (short-

dashed curve). The reflectivity values in this latter case are higher than the experimental ones, and the simulations that include ν_{neq} are clearly more relevant. On the subpicosecond time scale, the ionic temperature does not have enough time to increase because the energy transfer rate between electrons and ions has a characteristic time longer than τ_L. For the case $\nu_{neq}(N_e,T_e)=0$, the lattice remains cold during the laser pulse and the conductivity, depending on the electron-ion collision frequency, is close to the cold solid one. The p polarization shows a minimum reflectivity at closed to 59°. This minimum, which appears only for the p-polarization case, can be explained by the fact that for this polarization, the electromagnetic wave has a component colinear to the plasma density gradient.

The minimal reflectivity occurs for a calculated angle of approximately 59° which corresponds roughly to the experimental one. Eidmann *et al.* have already compared these experimental results with their hydrodynamic simulations which solve Helmholtz equation in a similar framework [20]. Nevertheless, their model does not consider contributions of $(e\text{-}e)$ collisions in the solid case, but the $(e\text{-}p)$ contribution was calculated with a different specific plasma model [20]. In this way, the collision frequency increased quickly during the laser pulse and they have found an angle corresponding to the minimal absorption around 70° in their calculations. They have imputed this discrepancy to the fact that they had not considered the depolarization in the calculation of the electromagnetic field. We have observed the same situation, where the angle of maximal absorption was overestimated with a pure p-polarized pulse. In our calculation, this overestimation was corrected by including a weak proportion of s-polarized wave in the total electromagnetic field. These simulations reveal a strong difference in the nature of the absorption of the s and p components of the heated matter absorption. When a density gradient is created at the metal surface, the simplest models used to calculate the electromagnetic fields at two interfaces or in the skin depth are no longer valid and it becomes necessary to solve the Helmholtz equation to calculate the deposited energy. Fedosejevs *et al.* have already indicated the importance of taking into account a correct density gradient to reproduce the experimental data. One-dimensional modeling appears to be sufficient to take into account the effects due to incident angle and polarization. Concerning the magnitude of the reflectivity, we have pointed out the crucial role of the correct conductivity by way of a total collision frequency including the $(e\text{-}e)$ collision rate. Moreover, the fact that the angle of minimal absorption was similar to the experiment shows that the hydrodynamics of the system is well reproduced by our simulations on the subpicosecond time scale.

In order to test our model on a second type of study, we have investigated the laser intensity dependence of these two polarizations while keeping constant the angle of incidence. The dependence of the reflectivity as a function of the intensity was experimentally studied by Milchberg *et al.* to determine the evolution of the aluminum resistivity during the solid-plasma transition when the change in density is weak [39]. These measurements were interpreted to provide an electronic temperature dependence for the resistivity. This dependence was studied for an aluminum target with a density close to the solid one for an intensity evolving for four orders of magnitude, from 5×10^{11} to 10^{14} W/cm^2. The reflectivity was determined by measuring the energy after reflection of the laser pulse which hits the target at an incident angle of 45°. The targets were prepared by depositing a 400-Å aluminum film on a glass substrates. The authors stated that for thicker film, the reflectivity remains constant.

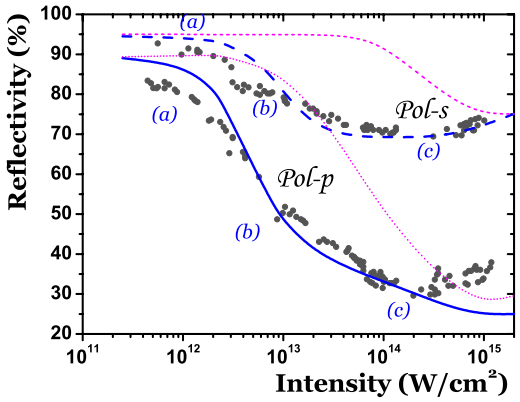

FIG. 3. (Color online) Simulated reflectivity as a function of intensity in an aluminum sample for s (dashed line) and p (solid line) polarization. Simulations performed with $\nu_{neq}=0$ are superposed for s (short-dashed line) and p (dotted line) polarization. Experimental data points (black dots) are taken from Milchberg *et al.* [39].

Figure 3 shows the experimental reflectivity associated with the 400-fs [full width at half maximum (FWHM)] s- and p-polarized incident pulses for fluences from 20 mJ/cm^2 to 2 kJ/cm^2 at $\lambda_\alpha=308$ nm. A decrease of reflectivity with intensity is observed. The challenge is to relate this decrease to an excitation model. The figure also shows the calculated result in two situations ($\nu_{neq}=0$, $\nu_{neq}\neq0$). Our simulations are in good agreement with these experimental measurements when the $(e\text{-}e)$ collisions are considered. Numerical calculations provide reflectivity evolutions based on the expression (5) where the upper limit of the integration time corresponds to the total pulse duration $\tau_L=1.2$ ps. A drop of reflectivity for an intensity range of 10^{12}–10^{15} W/cm^2 is observed. In the case $\nu_{neq}=0$, the dependences in T_i and N_e on the $(e\text{-}i)$ collisional processes are not sufficient to reproduce the experimental data and the agreement is poor. The drop in reflectivity occurs for higher intensities for both polarizations when the increase in ionic temperature starts to be important and to drive the absorption mechanism. This again shows the role of considered $(e\text{-}e)$ collision in influencing the transient optical properties.

Three regimes are clearly distinguishable when observing reflectivity as a function of the laser intensity. The reflectivity can be written as a function of the refractive index $\tilde{n}$ as $\mathcal{R}=|(1-\tilde{n})/(1+\tilde{n})|^2$, where, according to the Drude expression,

$$\tilde{n}^2(\omega_\alpha/\nu)=1+\frac{\omega_p^2}{\omega_\alpha^2}\frac{i\omega_\alpha/\nu}{1-i\omega_\alpha/\nu}, \tag{14}$$

where $\omega_p=(N_e e^2/m_e^\dagger\varepsilon_0)$ is the plasma frequency. The above equation used in the case of normal incidence of laser radia-

tion and the reflectivity at other incident angles for *p*- and *s*-polarized radiation can be calculated based on the Fresnel formulas. These considerations do not bring new information for a quantitative discussion, but allow a qualitative one. If $1 \leq \omega_\alpha/\nu \leq \omega_p/\nu$ with $\omega_\alpha = 6.12 \times 10^{15}$ s^{-1}, then $\tilde{n}^2 \simeq 1 + i\omega_p^2/\omega_\alpha \nu$ and $\overline{\mathcal{R}_\alpha}$ decreases with ν, corresponding to the first regimes. The first one, indicated by the label (*a*), is observable at intensities lower than a few 10^{12} W/cm^2. This regime, characterized by a reflectivity which decreases slowly, corresponds to an electronic temperature which is not sufficiently high to induce a high collision frequency ($\nu \ll \omega_\alpha$). Moreover, the energy exchange between electrons and ions is low and the matter remains in a solid state during the pulse duration. The $\overline{\mathcal{R}_\alpha}$ decrease is related to the rise of the (*e*-*i*) collision frequency, which depends almost linearly on the ionic temperature. Moreover, the decrease in density is weak in this regime and the reflectivity does not depend on the electronic density through ν and ω_p. The second regime, marked by the label (*b*) in Fig. 3, is reached for intensities between 10^{12} and 10^{14} W/cm^2. In this case, $\nu \simeq \omega_\alpha$ and the drop of $\overline{\mathcal{R}_\alpha}$ can be related to a strong T_e increase which leads to a frequency collision augmentation. In the assumption of the solid model, $\overline{\mathcal{R}_\alpha}$ decreases as $\nu_{neq} \propto T_e^2$, which corresponds to the regime put forward by Milchberg *et al.* in Ref. [39]. Note that the decrease in density starts to play a significant role in this regime as well and can induce a reduction of the reflectivity. Finally, for the highest intensities, the reflectivity remains constant or increases. This regime is more difficult to reproduce with simulations because, beyond 10^{14} W/cm^2, the experimental prepulse is sufficient to produce vapor or plasma before the absorption of the main pulse. In this case marked by the label (c), the electronic critical density reached in front of the aluminum sample yields a strong modification of the absorption properties. For the *p*-polarization case, $1 \ll \omega_p/\nu \leq \omega_\alpha/\nu$ and $\overline{\mathcal{R}_\alpha} \simeq (\omega_p/2\omega_\alpha)^2$ becomes low, depending on the electronic density.

The good agreement between the experimental and theoretical reflection factors shows the possibilities of using the model presented to reproduce and analyze the optical properties during the plasma formation induced by a laser pulse. This was achieved by properly estimating the collision frequency and other optical and thermodynamical parameters in nonequilibrium conditions. These results indicate that the numerical code is able to simulate the absorption of the incident electromagnetic wave in electron-ion nonequilibrium regimes. This provides opportunities to characterize the response of a material for time scales lower than the electron-ion relaxation time. We have studied reflectivities induced on a thick metal sample, where the heated matter at the surface was composed by a temporal sequence of several layers of different thermodynamic states. The next section is dedicated to specific experiments which allow to follow a single thermodynamic state on ultrashort time scales ensuring as well temporal resolution. Our simulations are suitable to provide precious information on the collisional processes and state of the system during its relaxation.

IV. APPLICATION TO THE PUMP-PROBE DIAGNOSTIC

Optical reflectivity and transmission measurements provide valuable insights into studying ultrafast phenomena in condensed matter and plasmas physics [18]. In particular, they enable observations of phase transitions and provide information about the transport properties of dense plasmas. If the resolution is short enough, pump-probe experiments are relevant to characterize the properties of the material during relaxation processes. The use of ultrashort laser pulse provides a subpicosecond resolution of the evolution after an ultrafast laser event: the pump excitation. The subsequent dynamics is then governed by the interactions among the elementary excitations and is monitored by using a second optical pulse: the probe. Reflectivity measurements strongly depend on plasma density and collision frequency. In these conditions, numerical investigations can provide the correlation between matter properties and relaxation process. In this section, we compare experimental results and simulations performed in similar conditions which permit us to split up the sequence of electron-electron, electron-phonon, and hydrodynamics relaxations.

A. Strong pulse and unperturbing probe

Our assumptions are first tested against the data points corresponding to pump-probe reflectivity and transmission experiment performed by Widmann *et al.* in Ref. [5]. In this case, the target is a gold foil with a thickness of about 28 nm which has been irradiated with a $\lambda_\alpha = 400$ nm, 150-fs (FWHM) laser pulse, at normal incidence. After focusing, the intensity of the pump pulse is about 10^{13} W/cm^2 on the metal surface. The reflectivity and the transmission of the initial solid and produced plasma are analyzed with an *s*-polarized probe pulse at $\lambda_\beta = 800$ nm with a similar duration, an incident angle of 45°, and a time delay varied from 0 to 15 ps after the pump pulse. In the experiment, reflected and transmitted energies were measured with photodiodes and compared to the incident energy to deduce an instantaneous reflectivity and transmission of the matter. In a similar way as in the previous section, simulated reflectivity $\overline{\mathcal{R}_\beta^s}(\delta t)$ and transmission $\overline{\mathcal{T}_\beta^s}(\delta t)[0,1]$ were calculated with expressions (5) and (6) where τ was taken to be equal to a variable time step $\delta t \leq 0.1$ fs.

At the beginning of the irradiation and at the probe frequency, solid gold shows a reflectivity of 93%. Following the irradiation, three regimes are clearly distinct in Fig. 4. The first one, shortly after the initial moment, is characterized by a swift decrease in both reflectivity and transmission during the first picosecond. The second one is marked by a plateau between 1 and 7 ps and corresponds to a regime where optical properties seems to be frozen because reflectivity and transmission are almost constant. Finally, a change appears after 7 ps and a last regime starts, characterized by a decrease in reflectivity and an increase in transmission. To explain these behaviors, we have performed five simulations with different configurations to identify the effect of the supposed main processes.

The first simulation labeled by (*a*) in Fig. 4 is a complete simulation including all the processes described in Sec. II and is used as the reference case to interpret the other calculations. The dash-dotted line (*b*) is a simulation without nonequilibrium contribution in the collision frequency. In this

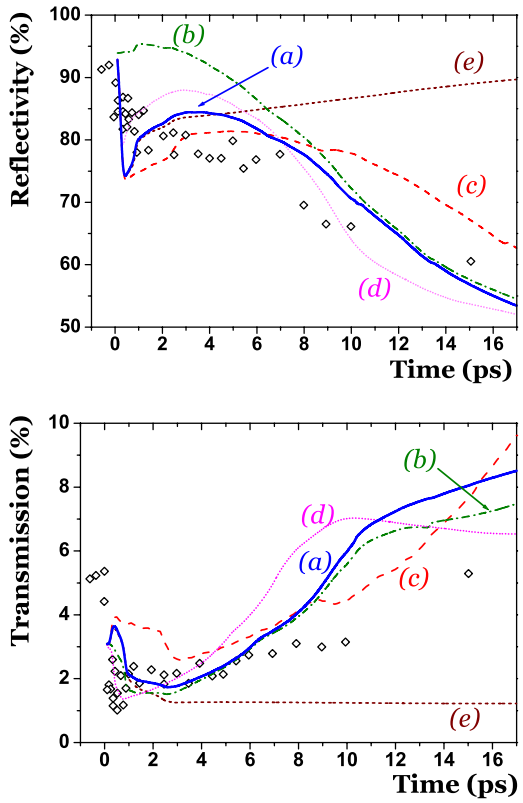

FIG. 4. (Color online) Numerical evolution (curves) of the reflectivity and the transmission of a 800-nm pulse probing a 28-nm gold foil thickness for different simulation configurations. The solid line (a) corresponds to the best-fitted complete simulation. The dash-dotted line (b) is a simulation without nonequilibrium contribution in the absorption. The dashed line (c) and the short-dotted line (d) correspond to simulations performed with a lower ($\gamma = \gamma_0/4$) and a higher ($\gamma = \gamma_0 \times 2$) e-p coupling term, respectively. The hydrodynamics processes have been switched off in the simulation shown by the short-dashed line (e). Experimental data points (black diamonds) are taken from Widmann *et al.* [5].

case, ν_{neq} contribution has been skipped from Eq. (8) and no (e-e) collision mechanism is taken into account in the bremsstrahlung absorption calculation. The expected difference has to take place during the nonequilibrium process, before electron-phonon thermalization. The calculated reflectivity is strongly different in the case (b) since the conductivity parameter only depends on the density and on the ionic temperature which evolves slowly compared to the electronic temperature variation. In contrast, curve (a) shows a drop in the reflectivity and reaches a minimum value at the end of the laser pump pulse, when the electronic temperature is maximal. At this time, $\Re_e[\tilde{\sigma}_\beta]$ and the subsequent quantity of absorbed energy are maximal. The transmission curve displays a less strong difference for these two cases because $\overline{\mathcal{R}_\beta}$ diminution and absorption increase occur simultaneously. For the case (a), as electrons transfer their energy to the ions, ν decreases and $\overline{\mathcal{R}_\beta}$ rises and reaches a maximal value at 4 ps. From this study, we can infer that the observed absorption in ultrafast time scales is mainly due to (e-e) collisions. Thus, during the electromagnetic excitation, the Coulomb interaction between electrons drives the Joule heating process.

The curves (c) and (d) include a nonequilibrium absorption mechanism, but differ from (a) in (e-p) energy transfer rate. In fact, the case (c) corresponds to a case where the usual (e-p) coupling term $\gamma_0 = 4 \times 10^{16}$ W K^{-1} m^{-3} has been divided by a factor of 4 to slow down the ionic temperature increase and to increase the nonequilibrium lifetime. Compared to the experimental data and the (a) reference case, the breakup with the third stage at 7 ps is smoothened and the region where the reflectivity remains constant is more pronounced. In contrast, for the (d) case, the (e-p) coupling term γ_0 was multiplied 5 times to accelerate the ionic temperature increase and to decrease the nonequilibrium lifetime. In this case, the length of the plateau (which is visible in both reflectivity and transmission) decreases and the equilibration time seems to be reduced. We deduce that the plateau can be attributed to the temperature equilibration mechanism between electrons and ions and the duration of this stage corresponds to the (e-p) relaxation time. After this, the hydrodynamics commences.

Finally, the fifth round (e) was performed by keeping $\gamma = \gamma_0$ as in (a), but the hydrodynamics processes have been stopped. To do this, the pressure p and the density ρ equal the standard pressure $p_0 = 10^{-5}$ Pa and the solid density $\rho_0 = 19.3$ g cm^{-3}, respectively, in the entire gold film. In this nonphysical case, no pressure gradient can cause motion, volume increase, surface expansion, or shock processes in the solid. The behavior of the optical properties is similar for (e) and (a) during the first 3–4 ps and, after this time, the reflectivity and transmission split and follow very different evolutions. In the isochoric case, the reflectivity increases continuously as the energy is transferred from the electrons to the ions. In fact, the total collision frequency ν decreases because the augmentation in (e-i) collision is not compensated by the (e-e) collision decrease. The transmission does not evolve anymore after the end of the nonequilibrium process since the change in reflectivity is compensated by a weaker absorption of the probe. In the hydrodynamic case (a), the reflectivity decreases because of the density decrease which is related to the plasma formation at the surface. In fact, according to the Spitzer formula and the Drude model for $\nu < \omega_\beta$, $\mathcal{R}_\beta$ decreases with the ionic temperature increase due to the increase in (e-i) collision frequency and $\overline{\mathcal{R}_\beta}$ decreases when the electron density drops. The change in $\tilde{\sigma}_\beta$ yields a greater skin depth for the probe, leading to increases in optical path length. As the plasma expands, the temperature and density fall and the free electrons recombine.

The experimental measurements were performed on a 30 ± 2 nm gold sample. The magnitude of absorption strongly depends on the material thickness. To estimate the influence on our simulations, Fig. 5 shows a dependence of the transient optical properties in the material thickness. In our simulation, an increase of energy of about 4.8×10^6 J/Kg given in Ref. [5] corresponds to an input fluence of 0.5 J cm^{-2} for the pump pulse incident on a sample of 28 nm thickness. The behavior of the reflectivity and transmission were investigated for three thicknesses of 28, 30, and 32 nm at the same fluence. These three simulations show that the general evolutions of the optical properties are identical

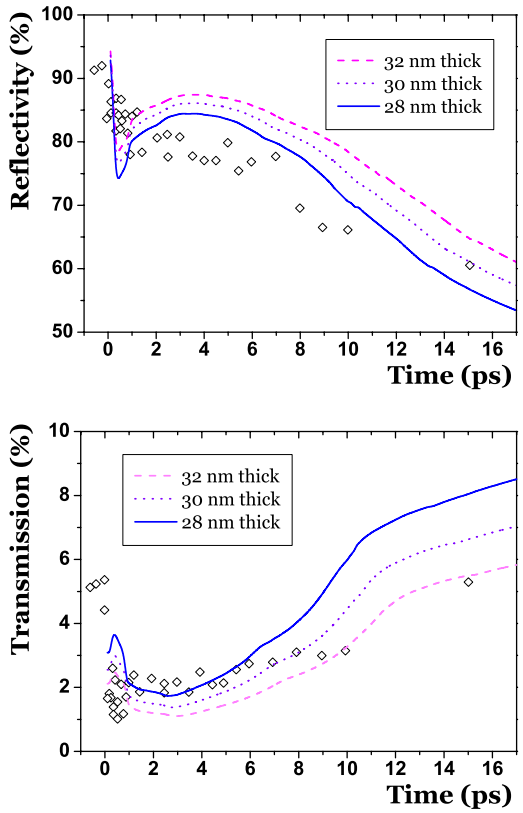

FIG. 5. (Color online) Time evolution of the reflectivity and the transmission of a 800-nm probe pulse for different thicknesses of a gold sample preexcited by a 400-nm laser pulse. Both behaviors exhibit an energy relaxation stage and solid to plasma transformation induced by a 400-nm, 0.5 J cm^{-2} pump pulse. Experimental data points (black diamonds) are taken from Widmann *et al.* [5]. Generation of nonequilibrium, relaxation to equilibrium, and solid to plasma transition is visible.

but differ in magnitude. The reflectivity increases whereas the transmission decreases with the film thickness. This simple result can give an explanation of the discrepancy between the experimental and simulated values in providing a kind of error bar to the numerical experiment data.

This numerical study emphasizes the role of the $(e\text{-}e)$ umklapp collision mechanism on the absorption of the laser pulse. The $(e\text{-}e)$ interaction influence the material optical response during a short time after the pump pulse. The following $(e\text{-}i)$ equilibration and the hydrodynamic stages have been identified as well. Due to the number of approximations in the optical model, the simulation does not perfectly match the experimental data. Nevertheless, the different phases of the matter evolution and the subsequent changes in the behavior of the optical properties are quite well reproduced. This numerical study, devoted to reflect the experimental conditions involving laser-metal irradiation for both pump and probe pulses, is an efficient tool to discriminate collisional processes. A direct interest of a low-energy probe pulse is the possibility of carrying out tests of optical absorption of the material. This study could be extended to perform temporal optimization of laser absorption in determining the time when the matter state is the more prepared and able to respond to the electromagnetic excitation.

B. Experiments under near-threshold laser excitation on solid samples

The final discussion relates to a class of pump-probe experiments which focus on particle emission. We propose a direct application of a double-pulse sequence in studying the consequence of transient optical properties on energy coupling efficiency as a function of delay. Experiments based on ion signal emission as a function of the time delay were performed on several metals [60]. The experiments map in time the energy deposition as a function of the delay between identical subthreshold pulses, the total energy being above the threshold. Here, the threshold is defined as ion emission threshold. This way a quantitative picture of the transient behavior of the energy coupled into the sample emerges. It is supposed that the energy density stored in the metal surface is strongly correlated on the ion emission [25]. A fast-decaying ion signal that drops to zero in the first hundreds of femtoseconds [60] was followed by a large peak of emission in the picosecond range [25,60,61].

To discuss the experimental results related to the time-varying ion signal, we have calculated the specific absorbed energy inside the skin depth in a metallic sample. We have chosen Al and Au as examples. The skin depth is defined as a time-dependent quantity, depending on the imaginary index which evolves with space and time. The laser irradiation is composed of two numerical identical pulses with a varying delay. We make the assumption that, to a certain extent, the energy density in the superficial layers determines the efficiency of phase transformation into a gas state and, therefore, particle emission [25]. The total specific absorbed energy (E_{sa}) of a 800-nm, 150-fs double pulse is then calculated as a function of time separation between the two pulses. We discuss two cases, Al and Au, for two reasons. The first reason is related to the different values of the $(e\text{-}p)$ coupling, Al showing an almost 10 times higher electron-phonon interaction strength. Second, Al shows a particular optical characteristic, with no significant change between solid and liquid phases at 800 nm [62]. The numerical experiments are carried away with two identical subthreshold pulses of 150 fs and 800 nm wavelength. The threshold is defined numerically by the onset of the gas-phase at 0.45 J cm^{-2} for Al and 2 J cm^{-2} for Au. The results are presented in Fig. 6. For both materials, the following particularities were noted.

Several characteristic stages are noticed with various peaks in the absorbed energy density. The first one appears during the first picosecond and shows a decay in the amount of energy stored E_{sa}, due to the decrease of $\Re_e[\tilde{\sigma}_\beta]$. This decay is faster for Al than for Au. Note that an important result not visible here is that simulations with a single pulse and a nonperturbing probe have revealed that the absorption increases strongly during the first pulse. This increase cannot be observed with an identical double-pulse experiment due to a convoluting effect. This increase is a consequence of the instantaneous T_e increase which yields a strong augmentation of the collision frequency. As T_e reaches its maximum, the absorption is maximal and the observed minimum is almost synchronized with the corresponding time. The electron-phonon energy transfer is responsible for the T_e decrease. As a consequence, T_e can be maximal at the end of the first

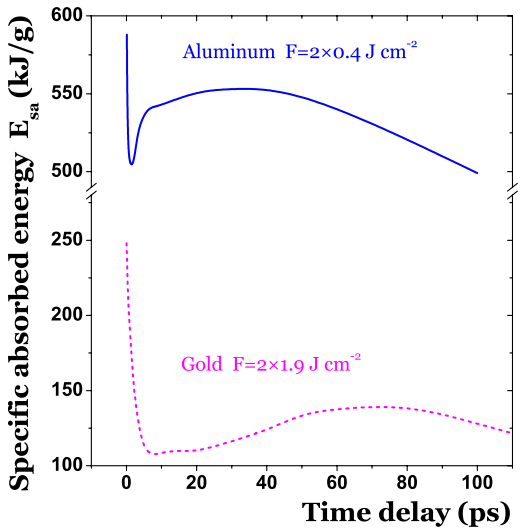

FIG. 6. (Color online) Calculated specific absorbed energy in the skin depth of an aluminum target irradiated by a double pulse (2×0.4 J cm^{-2}) and a gold target irradiated by a double pulse (2×1.9 J cm^{-2}). Simulations were performed as a function of time delay.

pulse if the electron-phonon coupling constant is very low. In the cases presented here, the absorption is maximal at about the half of the pulse duration, the corresponding time delay is close to the axis origin, and a fast decay occurs for short delay times. This variation is related to the T_e decrease which induces a drop of the collision frequency ν and a diminution of $\Re_e[\tilde{\sigma}_\beta]$. According to Eq. (7) in the range $\omega_\beta/\nu>1$, $\Re_e[\tilde{\sigma}_\beta]$ and the associated Joule heating process decrease as ν decreases. Moreover, a simulation performed, with setting $\nu_{neq}=0$, has shown that there is no decay for short time delay in this case. The electron-phonon energy transfer rate is correlated with the slope of the E_{sa} curve at short times. This slope is steeper for Al than for Au, and the decrease ends at 1.5 ps for Al and 6 ps for Au. A liquid phase is reached around 2 ps for Al and 7 ps for Au. The effect of the solid-liquid transition on the optical properties, which is expected to be more important for Au than for Al, is negligible because the nonequilibrium mechanism of absorption, especially (e-e) umklapp collisions, dominates. During this time, the ionic temperature T_i increases and the ν^{ei} increase results in an augmentation of $\Re_e[\tilde{\sigma}_\beta]$, balancing the effect of T_e decrease. At this stage, the optical properties are dominated by the ionic heating and T_i drives the absorption mechanism. After a single pulse, the thermalization is reached around 15 ps for Al and 50 ps for Au. T_i begins to decrease while ρ increases, prolonging the absorption increase. Note that the solidification process begins to occur at the rear side of the liquid layer. At 35 ps for Al and 75 ps for Au, solidification reaches the free surface of the liquid layer and ρ remains stable at solid density. The temperature decrease induces a drop of E_{sa} for longer time delays.

These simulations have shown that a fast decay in the absorbed energy can be imputed to the electronic temperature decrease and associated (e-e) effects during the nonequilibrium stage. Due to a smoother lattice heating, the fast decay is slower for Au than for Al. A recovery of the energy coupling efficiency on a tens of picoseconds scale is also observed for both materials. We have shown that the fact that the enhancement of optical absorption on a picosecond scale is due to an elevation of the ionic temperature. This enhancement happens earlier for Al because of a high electron-phonon coupling constant. Recondensation of matter into a high-density phase occurs after several tens of picoseconds and results in an E_{sa} drop. A similar situation was observed in experiments. As a conclusion, umklapp electron-electron collisions in the solid state determine the optical absorption behavior when the fluence is close to the threshold value.

V. CONCLUSION

Collisional absorption by inverse bremsstrahlung plays a major role in laser-matter interactions. The full description of inverse bremsstrahlung absorption requires knowledge of the electron-photon absorption mechanism and the associated umklapp electron-electron and electron-ion collision rates. We have conducted a simplified modeling of the optical properties to perform realistic simulations of several experiments present in the literature. We have used a relaxation-time model to approximate the two-body scattering rate. An important parameter determining the modification of laser-light absorption is the conductivity parameter, and we have proposed a description of its evolution during the material excitation. We used published results to test the hypothesis of an electronic contribution in a unified frame, covering various excitation stages, against its ability to explain experimental observations. In bringing together several accepted models in the solid and plasma ranges, a conductivity dependence of macroscopic properties such as electronic temperature (T_e), ionic temperature (T_i), and electronic density (N_e) was employed. This study is indicative of the potential role of electron-electron umklapp processes in optical absorption. An accurate evaluation of the umklapp rate would require complex kinetic approaches.

The numerical diagnostic that we have developed provide the correlation between the sequences of states of matter and the optical response. The information, resolved in time, gives insight into the relaxation mechanisms which drive the phase transitions and open new opportunities to monitor the excitation of a metal in controlling both its optical and thermal evolution. Several regimes of irradiation, including above and subthreshold regimes, were investigated. Clear modification of electronic and hydrodynamic effects was observed. Beyond the retrieval of the optical properties and the discussion of associated thermodynamic states, a qualitative idea on the transient energy coupling properties was given.

ACKNOWLEDGMENTS

The authors acknowledge the support of the GIP ANR and PICS programs.

[1] C.-K. Sun, F. Vallée, L. H. Acioli, E. P. Ippen, and J. G. Fujimoto, Phys. Rev. B **50**, 15337 (1994).
[2] R. H. M. Groeneveld, R. Sprik, and A. Lagendijk, Phys. Rev. Lett. **64**, 784 (1990).
[3] C. Guo, G. Rodriguez, A. Lobad, and A. J. Taylor, Phys. Rev. Lett. **84**, 4493 (2000).
[4] P. M. Norris, A. P. Caffrey, R. J. Stevens, J. M. Klopf, J. T. McLeskey, Jr., and A. N. Smith, Rev. Sci. Instrum. **74**, 400 (2003).
[5] K. Widmann, T. Ao, M. E. Foord, D. F. Price, A. D. Ellis, P. T. Springer, and A. Ng, Phys. Rev. Lett. **92**, 125002 (2004).
[6] C. W. Siders, A. Cavalleri, K. Sokolowski-Tinten, Cs. Toth, T. Guo, M. Kammler, M. Horn von Hoegen, K. R. Wilson, D. von der Linde, and C. P. J. Barty, Science **286**, 1340 (1999).
[7] B. J. Siwick, J. R. Dwyer, R. E. Jordan, and R. J. D. Miller, Science **302**, 1382 (2003).
[8] G. L. Eesley, Phys. Rev. B **33**, 2144 (1986).
[9] W. S. Fann, R. Storz, H. W. K. Tom, and J. Bokor, Phys. Rev. Lett. **68**, 2834 (1992).
[10] H. E. Elsayed-Ali, T. B. Norris, M. A. Pessot, and G. A. Mourou, Phys. Rev. Lett. **58**, 1212 (1987).
[11] R. W. Schoenlein, W. Z. Lin, J. G. Fujimoto, and G. L. Eesley, Phys. Rev. Lett. **58**, 1680 (1987).
[12] S. D. Brorson, A. Kazeroonian, J. S. Moodera, D. W. Face, T. K. Cheng, E. P. Ippen, M. S. Dresselhaus, and G. Dresselhaus, Phys. Rev. Lett. **64**, 2172 (1990).
[13] N. K. Sherman, F. Brunel, P. B. Corkum, and F. A. Hegmann, Opt. Eng. **28**, 1114 (1989).
[14] D. Bejan and G. Raseev, Phys. Rev. B **55**, 4250 (1997).
[15] V. E. Gusev and O. B. Wright, Phys. Rev. B **57**, 2878 (1998).
[16] B. Rethfeld, A. Kaiser, M. Vicanek, and G. Simon, Phys. Rev. B **65**, 214303 (2002).
[17] P. Celliers and A. Ng, Phys. Rev. E **47**, 3547 (1993).
[18] A. Ng, A. Forsman, and G. Chiu, Phys. Rev. Lett. **81**, 2914 (1998).
[19] A. M. Komashko, M. D. Feit, A. M. Rubenchik, M. D. Perry, and P. S. Banks, Appl. Phys. A: Mater. Sci. Process. **69**, Suppl., S95 (1999).
[20] K. Eidmann, J. Meyer-ter-Vehn, T. Schlegel, and S. Hüller, Phys. Rev. E **62**, 1202 (2000).
[21] S. I. Anisimov, B. Kapeliovich, and T. L. Perel'man, Sov. Phys. JETP **39**, 375 (1974).
[22] M. I. Kaganov, I. M. Lifshitz, and M. V. Tanatarov, Sov. Phys. JETP **4**, 173 (1957).
[23] S. I. Anisimov and B. S. Luk'yanchuk, Usp. Fiz. Nauk **172**, 301 (2002) [Phys. Usp. **45**, 293 (2002)].
[24] J. P. Colombier, P. Combis, F. Bonneau, R. Le Harzic, and E. Audouard, Phys. Rev. B **71**, 165406 (2005).
[25] J. P. Colombier, P. Combis, A. Rosenfeld, I. V. Hertel, E. Audouard, and R. Stoian, Phys. Rev. B **74**, 224106 (2006).
[26] Y. T. Lee and R. M. More, Phys. Fluids **27**, 1273 (1984).
[27] F. Perrot and M. W. C. Dharma-wardana, Phys. Rev. A **36**, 238 (1987).
[28] M. P. Desjarlais, J. D. Kress, and L. A. Collins, Phys. Rev. E **66**, 025401(R) (2002).
[29] G. Faussurier, C. Blancard, P. Renaudin, and P. L. Silvestrelli, Phys. Rev. B **73**, 075106 (2006).
[30] A. V. Lugovskoy, T. Usmanov, and A. V. Zinoviev, J. Phys. D **27**, 628 (1994).
[31] A. V. Lugovskoy and I. Bray, Phys. Rev. B **60**, 3279 (1999).
[32] V. P. Silin and S. A. Uryupin, Zh. Eksp. Teor. Fiz. **81**, 910 (1981) [Sov. Phys. JETP **54**, 485 (1981)].
[33] T. Bornath, M. Schlanges, P. Hilse, and D. Kremp, Phys. Rev. E **64**, 026414 (2001).
[34] W. W. Schulz and P. B. Allen, Phys. Rev. B **52**, 7994 (1995).
[35] B. Hüttner, J. Phys.: Condens. Matter **6**, 2459 (1994).
[36] D. Fisher, M. Fraenkel, Z. Henis, E. Moshe, and S. Eliezer, Phys. Rev. E **65**, 016409 (2001).
[37] N. W. Ashcroft and N. D. Mermin, *Solid State Physics* (Harcourt Brace, Fort Worth, TX, 1976).
[38] R. Fedosejevs, R. Ottmann, R. Sigel, G. Künle, S. Szatmari, and F. P. Schäfer, Phys. Rev. Lett. **64**, 1250 (1990).
[39] H. M. Milchberg, R. R. Freeman, S. C. Davey, and R. M. More, Phys. Rev. Lett. **61**, 2364 (1988).
[40] H. Ki, P. S. Mohanty, and J. Mazumder, J. Phys. D **34**, 364 (2001).
[41] C. Schäfer, H. M. Urbassek, and L. V. Zhigilei, Phys. Rev. B **66**, 115404 (2002).
[42] T. E. Itina, J. Hermann, Ph. Delaporte, and M. Sentis, Thin Solid Films **453–454**, 513 (2004).
[43] P. Lorazo, L. J. Lewis, and M. Meunier, Phys. Rev. B **73**, 134108 (2006).
[44] A. V. Bushman, I. V. Lomonosov, and V. E. Fortov, Sov. Technol. Rev. B **5**, 1 (1993).
[45] J. P. Colombier, P. Combis, R. Stoian, and E. Audouard, Phys. Rev. B **75**, 104105 (2007).
[46] D. J. Steinberg, S. G. Cochran, and M. W. Guinan, J. Appl. Phys. **51**, 1498 (1980).
[47] E. Palik, *Handbook of Optical Constants of Solids* (Academic Press, London, 1985).
[48] W. Ebeling, A. Förster, V. Fortov, V. Griaznov, and A. Polishchuk, *Thermophysical Properties of Hot Dense Plasmas* (Teubner, Stuttgart, 1991).
[49] A. W. DeSilva and J. D. Katsouros, Phys. Rev. E **57**, 5945 (1998).
[50] A. A. Abrikosov, *Fundamentals of the Theory of Metals* (North-Holland, Amsterdam, 1988).
[51] W. E. Lawrence and J. W. Wilkins, Phys. Rev. B **7**, 2317 (1973).
[52] G. R. Parkins, W. E. Lawrence, and R. W. Christy, Phys. Rev. B **23**, 6408 (1981).
[53] A. H. MacDonald, Phys. Rev. Lett. **44**, 489 (1980).
[54] M. Kaveh and H. Wiser, Adv. Phys. **33**, 257 (1984).
[55] R. H. M. Groeneveld, R. Sprik, and A. Lagendijk, Phys. Rev. B **51**, 11433 (1995).
[56] C. Voisin, D. Christofilos, P. A. Loukakos, N. Del Fatti, F. Vallée, J. Lermé, M. Gaudry, E. Cottancin, M. Pellarin, and M. Broyer, Phys. Rev. B **69**, 195416 (2004).
[57] R. M. More, K. H. Warren, D. A. Young, and G. B. Zimmerman, Phys. Fluids **31**, 3059 (1988).
[58] E. Martinolli *et al.*, Phys. Rev. E **73**, 046402 (2006).
[59] N. W. Ashcroft and K. Sturm, Phys. Rev. B **3**, 1898 (1971).
[60] V. Schmidt, W. Husinsky, and G. Betz, Phys. Rev. Lett. **85**, 3516 (2000).
[61] R. Stoian, A. Rosenfeld, D. Ashkenasi, I. V. Hertel, N. M. Bulgakova, and E. E. B. Campbell, Phys. Rev. Lett. **88**, 097603 (2002).
[62] S. Krishnan and P. C. Nordine, Phys. Rev. B **47**, 11780 (1993).